AVO processing of walkaway VSP data at Ross Lake heavy oilfield, Saskatchewan

Zimin Zhang, Robert R. Stewart, and Don C. Lawton

ABSTRACT

The AVO processing and analysis of walkaway VSP data at Ross Lake heavy oilfield, Saskatchewan is described in this report. A walkaway VSP geometry has advantages for AVO analysis: True amplitude processing is feasible and undesired wave-propagation effects can be minimized. At the top and the base of the target channel sand, the synthetic seismogram and walkaway VSP processing results show a similar amplitude variation with offset for the reflections of both PP and PS waves. These results indicate the promise of rock properties inversion using AVO gather from walkaway VSP.

INTRODUCTION

Due to its geometry, a VSP survey has some advantages for AVO analysis (Coulombe et al., 1996): (1) VSP data generally have a broader bandwidth than comparable surface seismic data due to the short travel path from the source to receiver, especially only one-way through the near surface; (2) the S/N (signal-to-noise ratio) is higher than that of surface seismic data due to the quiet borehole environment; (3) a deterministic waveshaping deconvolution operator can be designed because the downgoing wavefield is also recorded, thus wave-field propagation effects such as multiples and attenuation along the incident travel path can be removed; (4) the downgoing (incident) waves and upgoing (reflected) waves are both recorded near the interface and largely free of undesirable wave propagation effects, thus a good estimate of the reflection coefficient of an interface is relatively easy to obtain. The walkaway VSP geometry is especially suitable for AVO analysis. FIG 1 shows how a walkway VSP geometry can be used to record data specifically for AVO analysis of a reservoir zone. The source positions of the walkaway VSP are located at increasing offsets from the borehole to obtain seismic reflections over a range of incident angles. By locating the receiver directly above the reflector, the same reflection point is imaged by each source position and the reflection travel path is short to minimize undesired wave-propagation effects. In relatively flat geological areas, the reflection travel path is small and the reflection point is close to the borehole when the receiver is near the reflector. Seismic reflection coefficients can be obtained by taking the ratio of the incident and reflected wave amplitudes. A direct-arrival raypath and reflection raypath for an arbitrary interface are shown in FIG 1. The amplitude of the recorded P-wave direct arrival and the amplitude of the P-wave incident on the interface are approximately equal as they have nearly identical travel paths. The ratio between recorded upgoing (reflected) and downgoing wave amplitudes is a good approximation to the band-limited reflection coefficient of the interface. This ratio is independent of most wave-propagation effects such as attenuation, transmission losses, multiples and spherical spreading, since the travel path of the reflected wave is small, and the travel paths of the two downgoing P-waves are approximately the same. This ratio process also removes source directivity

and source or receiver coupling effects, as the reflection amplitude is normalized by the amplitude of the incident wave.

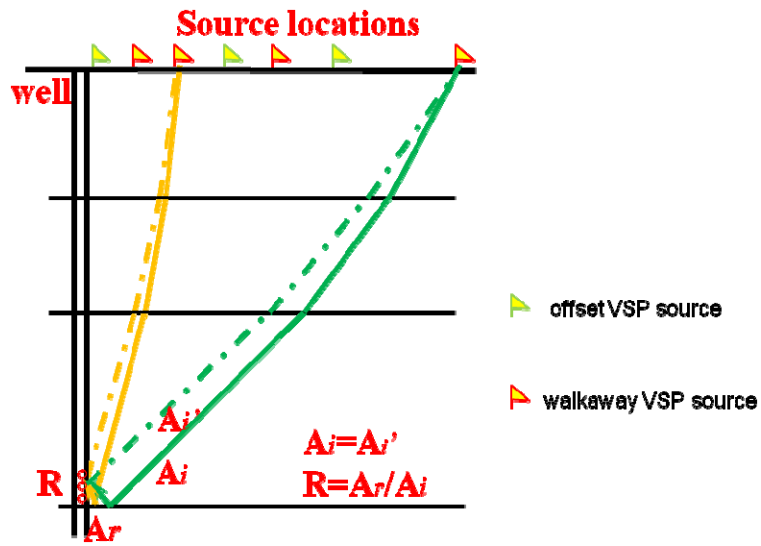

FIG 1. Schematic diagram of the advantage of walkaway VSP geometry for AVO processing. Since the receivers are located very close to the reflectors, the incidence wave amplitude *Ai* approximately equal to the downgoing wave amplitude A_i'. Thus the reflectivity *R* can be calculated by dividing the upgoing wave amplitude *Ar* by downgoing wave amplitude A_i. Shots at varied locations give different incidence angles, therefore AVO gather can be built.

Considering all these advantages, walkaway VSP data were acquired and processed for AVO analysis at the reservoir interval at the Ross Lake, Saskatchewan. The Ross Lake heavy oilfield (operated by Husky Energy Inc.) is located in south-western Saskatchewan. The exploration target is the Cretaceous channel sand in the Dimmock Creek member of the Cantuar Formation of the Mannville Group. The Mannville Group sandstones and shales unconformably overlie Jurassic sediments, and underlie the Joli Fou Formation of the Colorado Group. The Cantuar Formation of the Mannville Group is composed mostly of sediment developed within ancient valley systems (Christopher, 1974), which carved into the Success Formation and the Upper Jurassic Vanguard Group (FIG 2). The channel sands in the Dimmock Creek member have high porosities, of about 30%, and very high permeability (up to the 3 Darcy range). The produced oil is about 13° API gravity.

For detailed mapping of the Cantuar Formation channel reservoir, the CREWES Project, Husky Energy Inc., and Schlumberger Canada conducted a multi-offset VSP survey in well 11-25-13-17W3 in June 2003, to enhance the interpretation of surface 3C-3D seismic survey acquired in 2002. The locations of the VSP source and the well are shown in FIG 3. All the surveys were conducted with a downhole five-level, three-component VSP tool. The zero-offset VSP survey used both vertical and horizontal (inline) vibrators as sources. A vertical vibrator only was used for the far-offset VSP surveys, and the walkaway VSP surveys. The processing of offset VSP

data was previously described by Zhang and Stewart (2007). In this report, AVO processing and analysis of walkaway VSP data are described.

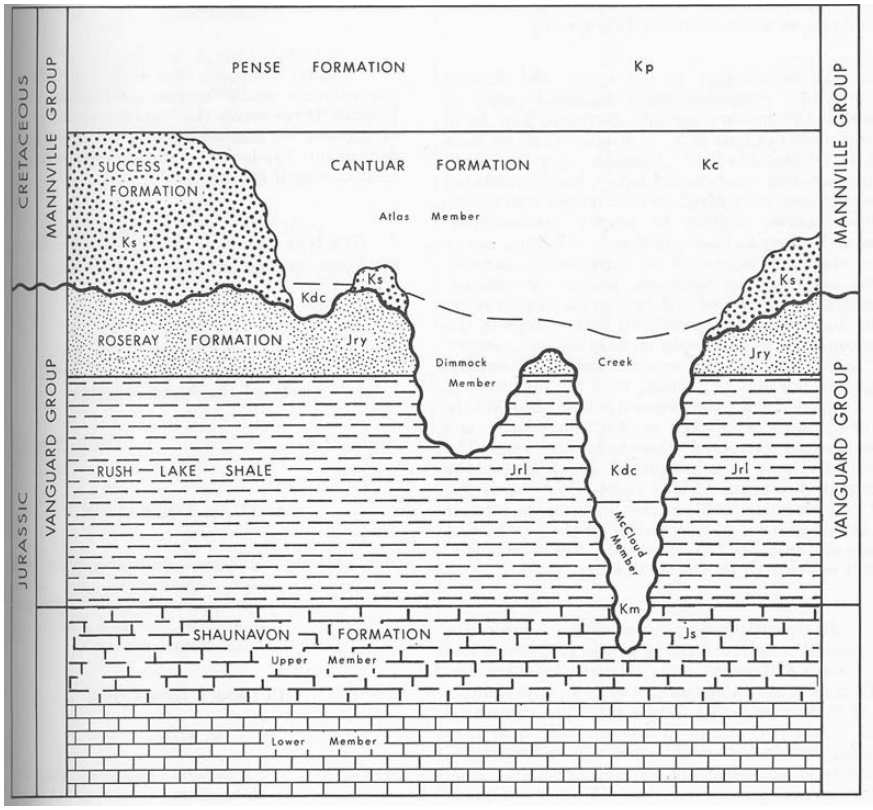

FIG 2. Stratigraphic relationship of the upper Jurassic and Lower Cretaceous sediments from southwestern Saskatchewan (from Christopher, 1974).

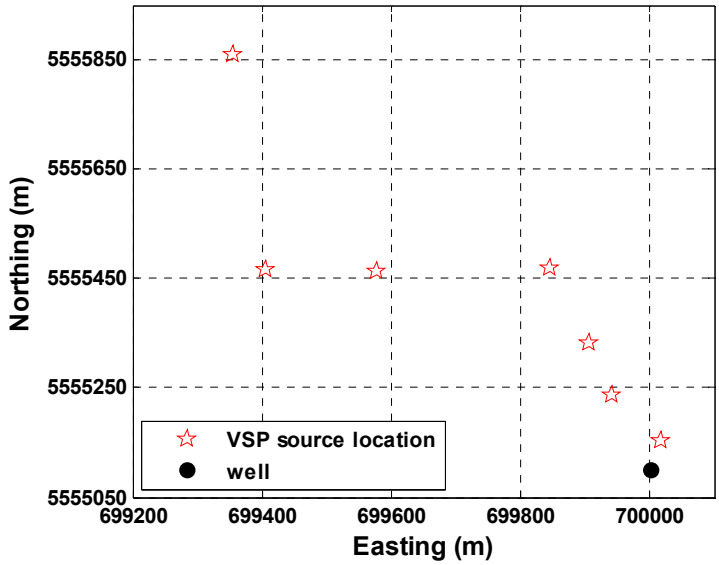

FIG 3. Locations of the well and VSP sources.

In addition to the four source locations of the walkaway survey, the zero-offset VSP and two far-offset VSP data sets were also processed using the same workflow and included in the AVO analysis. The source and receiver locations for these VSP shots are listed in Table 1. The top receiver of the walkaway VSP is 954m, which is above the Viking Formation and within the Lower Colorado Group. The top of the studied reservoir sand is approximately 1048m from the surface. The bottom receiver of all the VSP shots is in the channel sand.

Table 1.VSP surveys for walkaway VSP processing.

Survey Type	*Source Offset (m)*	*Number of Receivers*	*Top Receiver Depth (m)*	*Bottom Receiver Depth (m)*	*Receiver Spacing (m)*
Zero Offset	54	130 (14)	197 (954.5)	1165	7.5 (15)
Offset	399	130 (14)	197 (954.5)	1165	7.5 (15)
	699	130 (14)	197 (954.5)	1165	7.5 (15)
Walkaway	150	14	954.5	1165	15
	250	14	954.5	1165	15
	558	14	954.5	1165	15
	997	14	954.5	1165	15

Note: the numbers parenthesized in the table are the values actually used for AVO processing.

PROCESSING THE WALKAWAY VSP DATA

The walkaway VSP data were processed using a workflow described by Coulombe et al. (1996, as shown in FIG 4). The processing of the 558 m offset will be used as an example to illustrate the processing procedure. First, each shot was processed individually with a workflow similar to that for offset VSP. Horizontal rotation (described in appendix) was applied initially to correct for tool spin. The resultant Hmax (horizontal radial direction) and Hmin (horizontal transverse direction) for the 558 m offset VSP are shown in FIG 5. Upgoing and downgoing P and SV waves were separated from Hmax and Z component data by “wave-by-wave” algorithm (Blias, 2007). A significant merit of the “wave-by-wave” algorithm compared with a conventional median filter or FK filter methods is that the separated wavefields are largely noise free. FIG 6 displays the downgoing and upgoing P waves, and SV waves, derived from the Hmax and Z component data. Then deterministic deconvolution was applied to the upgoing wavefield using the deconvolution operator designed on the downgoing P wave for each shot. FIG 7 shows the comparison of the downgoing P wave before and after deconvolution, respectively. After deconvolution, the downgoing P wave was compressed to a real zero-phase wavelet, its corresponding amplitude spectrum was whiter that for the raw data. The deconvolved upgoing P and SV waves using the operator designed form downgoing waves are shown as FIG 8.

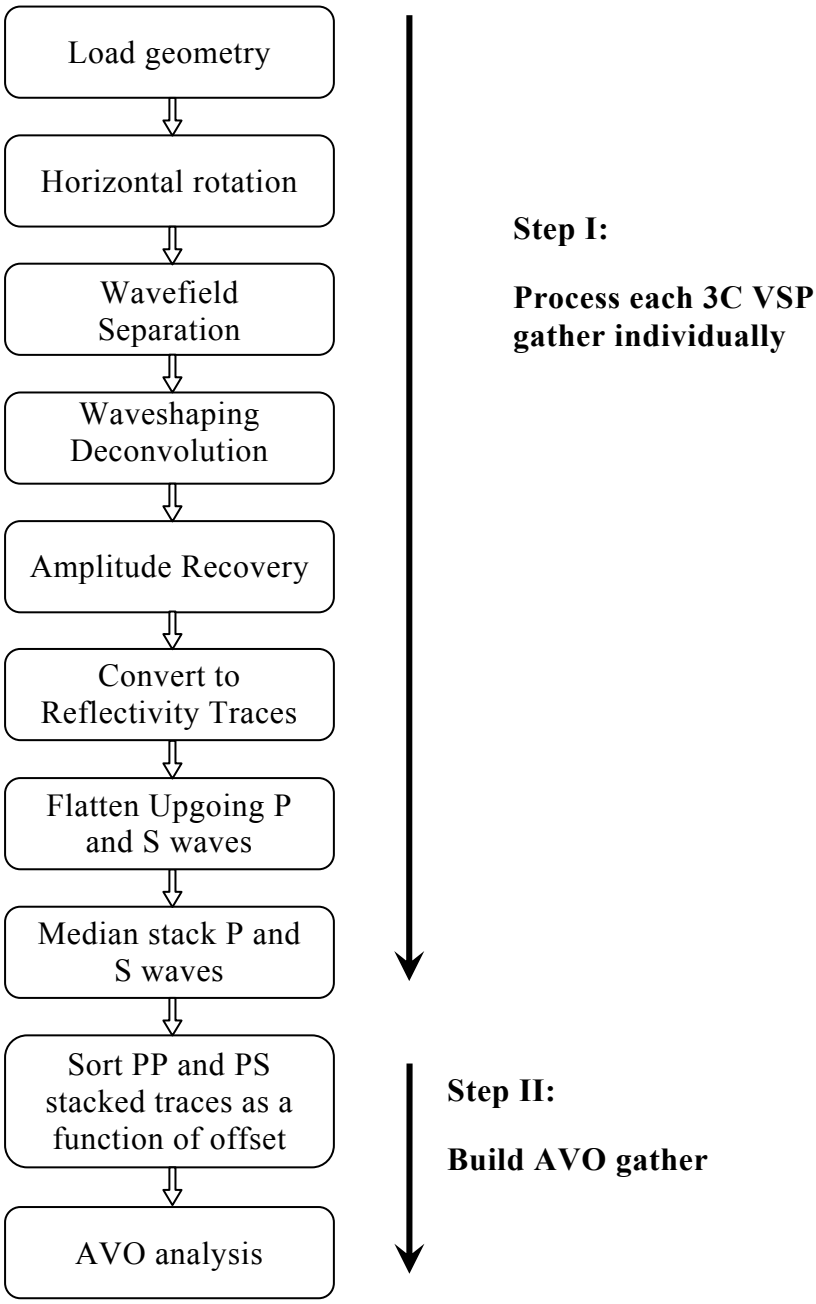

FIG 4. The walkaway VSP processing workflow for AVO analysis (modified after Coulombe et al., 1996). Each offset was processed individually to get a reflectivity trace from each shot, and then all shots were combined to form an offset-dependent gather for AVO analysis.

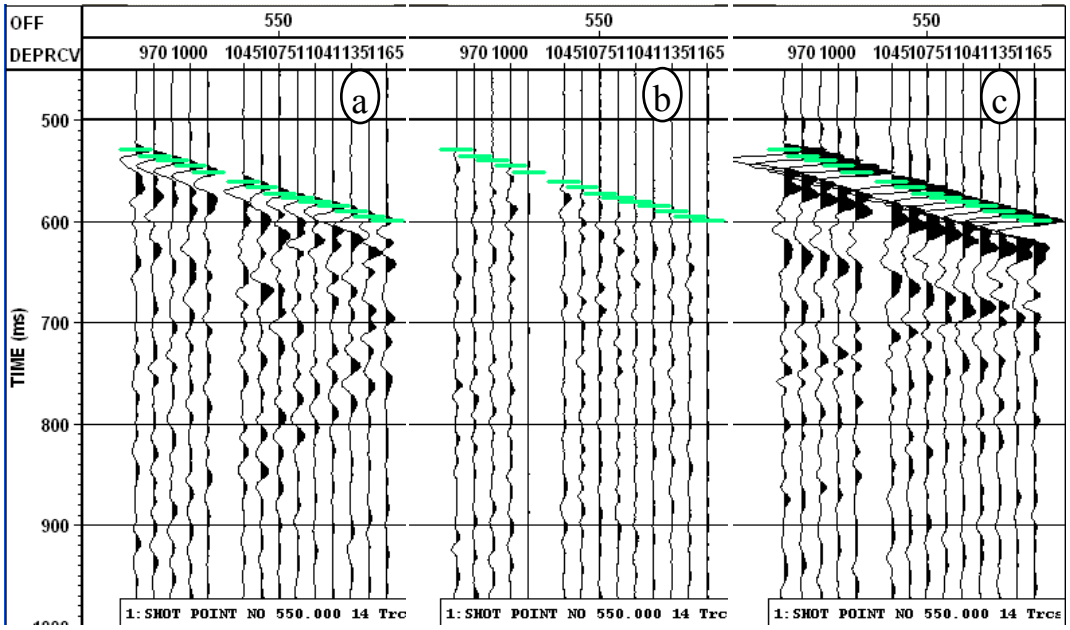

FIG 5. Hmax (a, horizontal radial), Hmin (b, horizontal transverse) after a horizontal rotation of X and Y components, and Z component data (c) of the offset 558 m shot (AGC applied, the green line is the first break picks). The waves received in transverse direction (Hmin) are much weaker than those in the radial direction (Hmax).

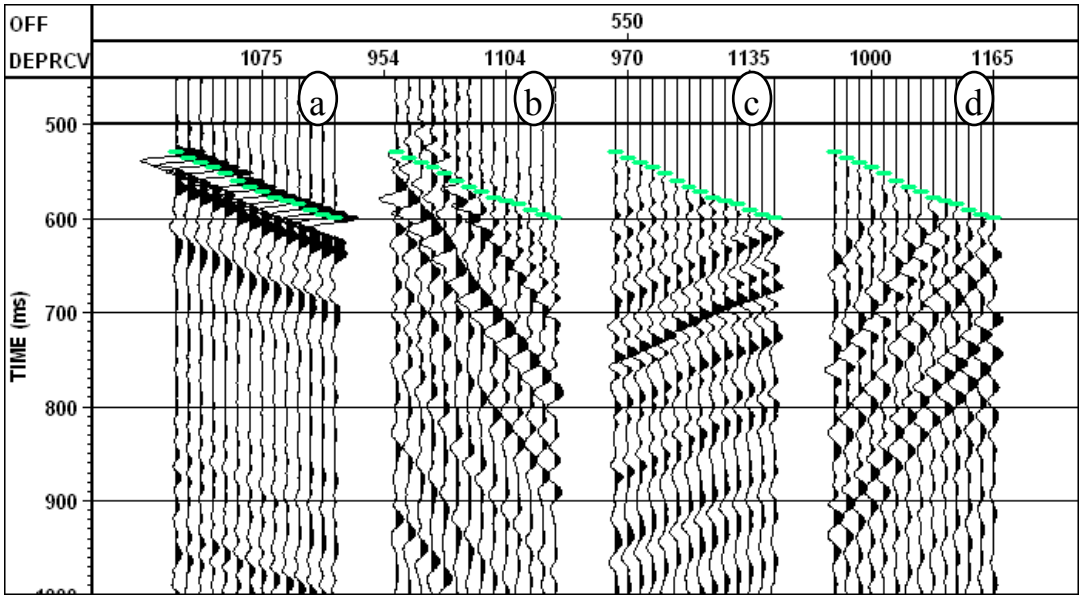

FIG 6. Downgoing P waves (a), downgoing SV waves (b), upgoing P waves (c), and upgoing SV waves (d) separated from Hmax and Z data of the offset 558 m shot (AGC applied, the green line indicates the first arrival picks).

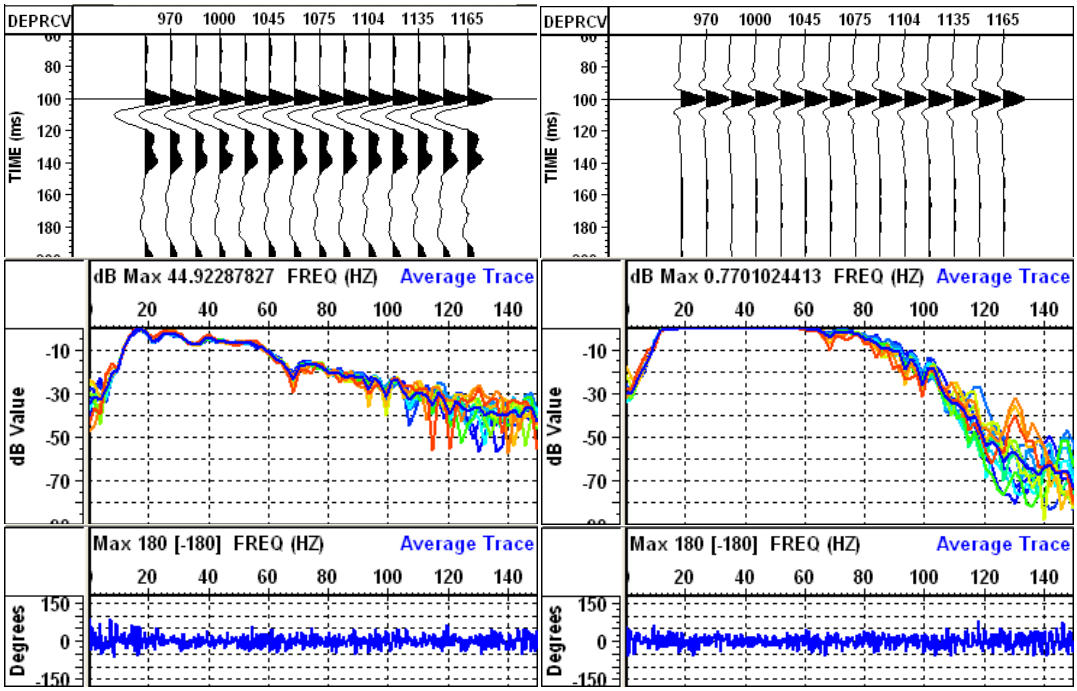

FIG 7. Downgoing P waves before (top left) and after (top right) deterministic deconvolution, as well as the corresponding amplitude spectra (the average spectrum is in blue) and average phase spectra (shot offset 558 m).

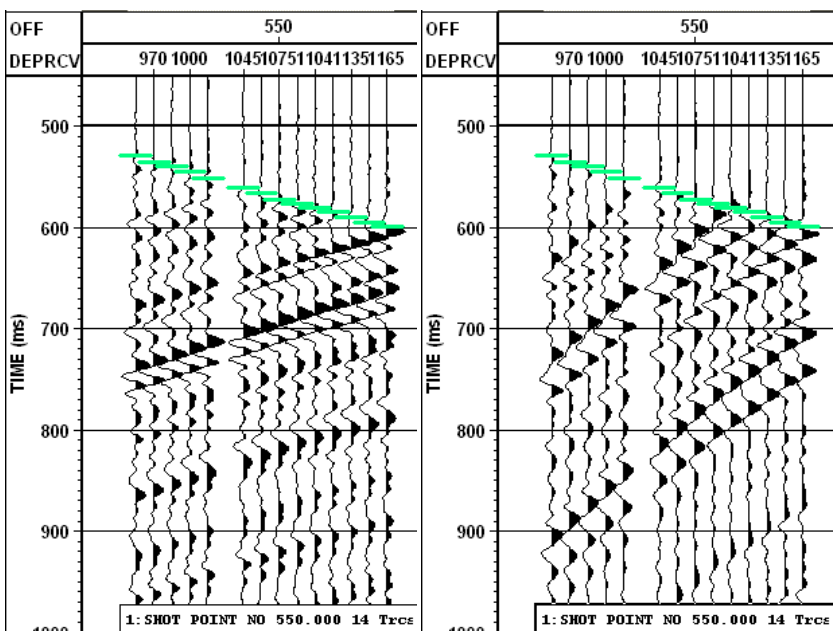

FIG 8. Upgoing P and SV waves after a deterministic deconvolution with operator derived from downgoing P waves (shot offset 558 m, the green line indicates first arrival picks).

To recover the true amplitudes for the P- and S-waves, scale factors were first calculated by normalizing the downgoing P waves and applied to the upgoing P and shear wavefields. This processing compensates for the energy decay during the downward propagation; thus the incident waves will be at the same relative

amplitude level at each depth level. FIG 9 displays the mean scaling of downgoing P waves. Before scaling, the P wave amplitude decreases with depth but after mean scaling over a window from 90 ms to 110 ms, the downgoing P wave at each receiver depth was normalized to the same amplitude. Then a $t^{1.6}$ gain was used to correct spherical divergence losses. The final step for amplitude processing was dividing the upgoing wavefield by the peak amplitude of the downgoing P wave to get the reflectivity traces. FIG 10 displays the upgoing P and SV offset-dependent reflectivity gather at a receiver depth 1075 m, from the seven VSP shots.

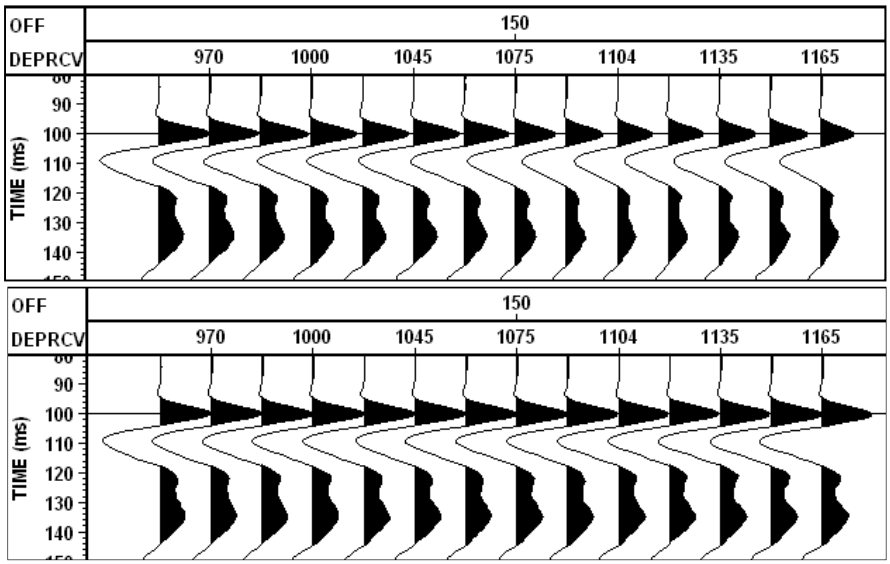

FIG 9. Downgoing P waves before and after mean scaling (flattened to 100 ms, shot offset 558 m). Note amplitude decay of direct P waves with increasing receiver depth before scaling.

After amplitude processing, NMO correction was applied to each shot. Also the traces were flattened to the reflection time of a specific event to remove the effect of small time shifts between each trace due to source statics. Here the reflection of the base of the sand channel was chosen, considering that it is close to the reservoir and its reflection is strong and easy to pick. The two-way P wave traveltime was determined after applying NMO correction and first-arrival time flattening of the upgoing P wavefield of the zero-offset VSP. This process will also correct the static due to source elevation and near surface velocity variation between each shot. The reflection of the same horizon, the base of sand channel was corrected to 1096 ms for every VSP shot and the results are shown as FIG 11.

Finally, the upgoing P and S waves from each shot were stacked as one trace to improve the signal-to-noise ratio, and were then sorted into offset-dependent gathers for AVO analysis. FIG 12 shows the offset gather from common shot stack of the upgoing wavefield, flattened to the reflection time of the base of the sand channel. NMO exists between the shots at different offset locations. The PP reflection time difference on stacked traces between offset 54 m and 699 m is 10 ms for the high-amplitude peak at about 1.15 s. The PS time difference for the same horizon is about 12 ms at about 1.2 s. Combining NMO and channel base reflection flattening, the

time shift between different offset locations was removed (FIG 11). FIG 13 shows the stack P and SV traces sorted in the order of source offset. Compared with the results shown in FIG 12, the time shift between traces caused by NMO is basically removed not only for the reflection of the channel sand base but for the reflections of other interfaces, too.

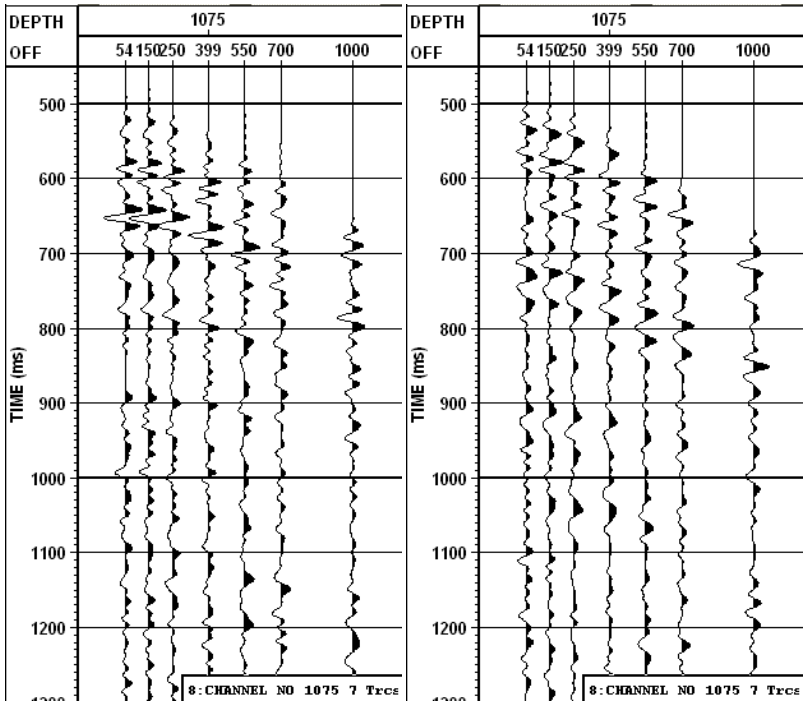

FIG 10. Upgoing P and SV offset-dependent reflectivity gather at a receiver depth of 1075 m.

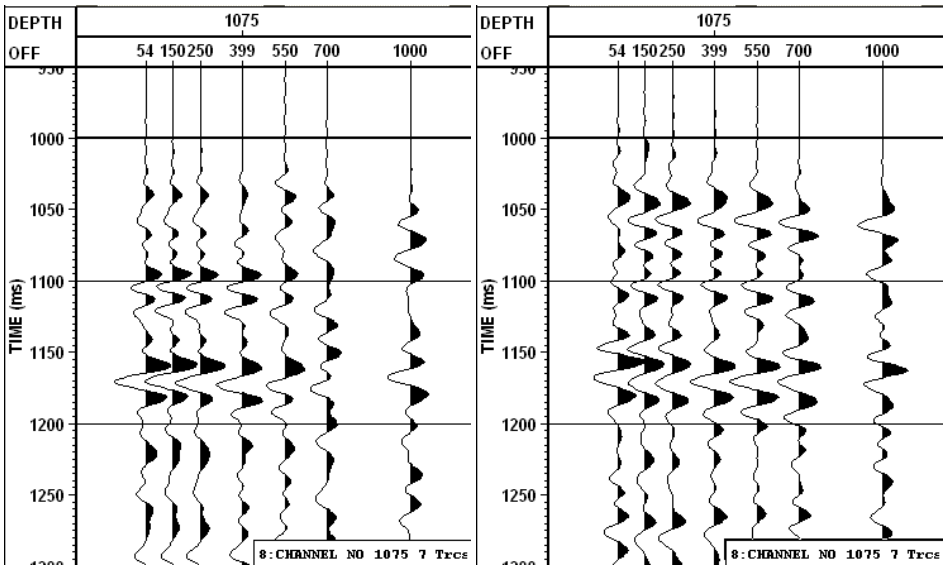

FIG 11. NMO and static correction (by flattening the 1096 ms event) applied to an upgoing P and SV offset-dependent reflectivity gather at a receiver depth of 1075 m.

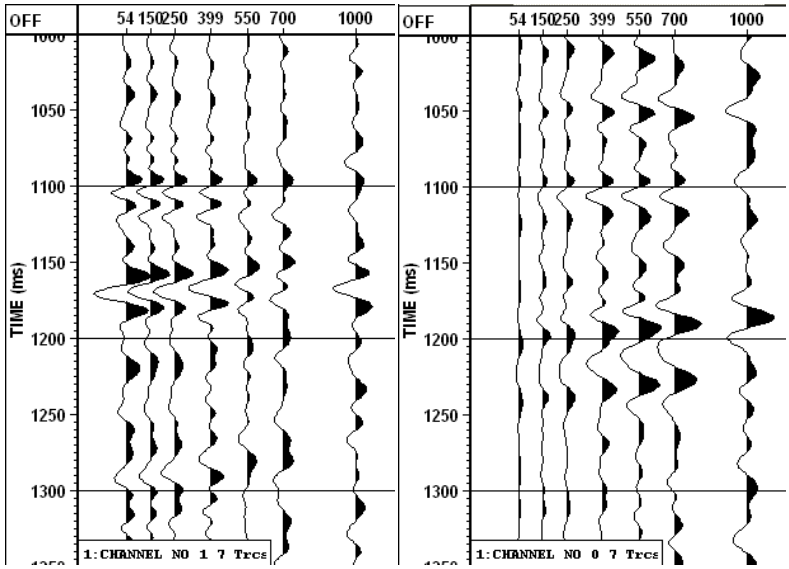

FIG 12. Offset gathers of upgoing P and upgoing SV waves from the common shot stack of 1096 ms event flattened gathers (no NMO correction). Note that only the 1096 ms reflection was exactly flattened, the other reflections were all dipping toward 1096 ms event.

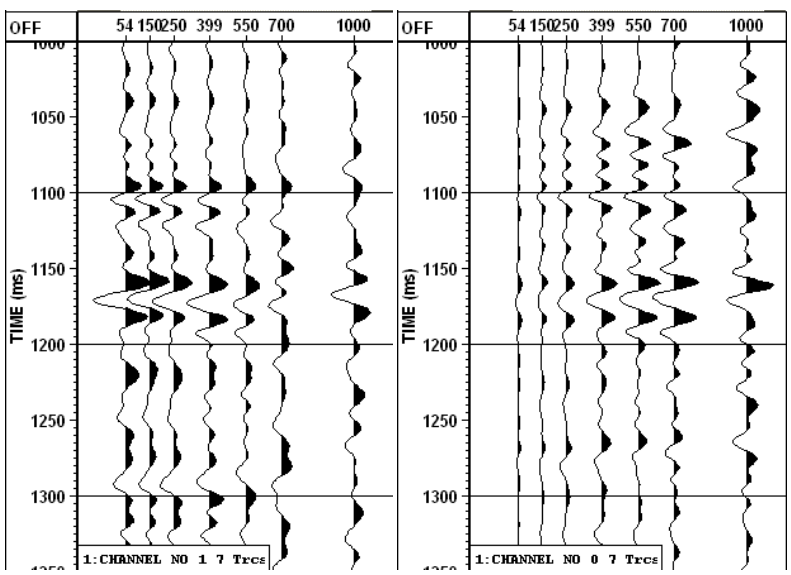

FIG 13. Offset gathers of upgoing P and upgoing SV waves from the common shot stack after NMO and static correction (by flattening the 1096 ms event). SV wavefield (P-SV) was also converted to PP reflection time.

Mean scaling factors calculated from the downgoing P wave were applied to the upgoing wavefields to account for incident wave amplitude decay due to increasing propagation distance. However, it is only accurate for the reflections recorded at the receivers very close to the reflectors. Furthermore, spherical divergence and transmission losses were also very difficult to be fully compensated. However, for reflections recorded by receivers close to reflectors, the amplitude recovery measures used are effective and accurate. Therefore a corridor stack will yield more reliable reflectivity traces. FIG 14 displays the corridor mute of upgoing P and SV waves.

We find that the amplitude of each event on the corridor muted traces is fairly consistent at different depths. Then, each shot was stacked and sorted to offset-dependent gathers for AVO analysis (the P and SV offset-dependent reflectivity traces are shown in FIG 15).

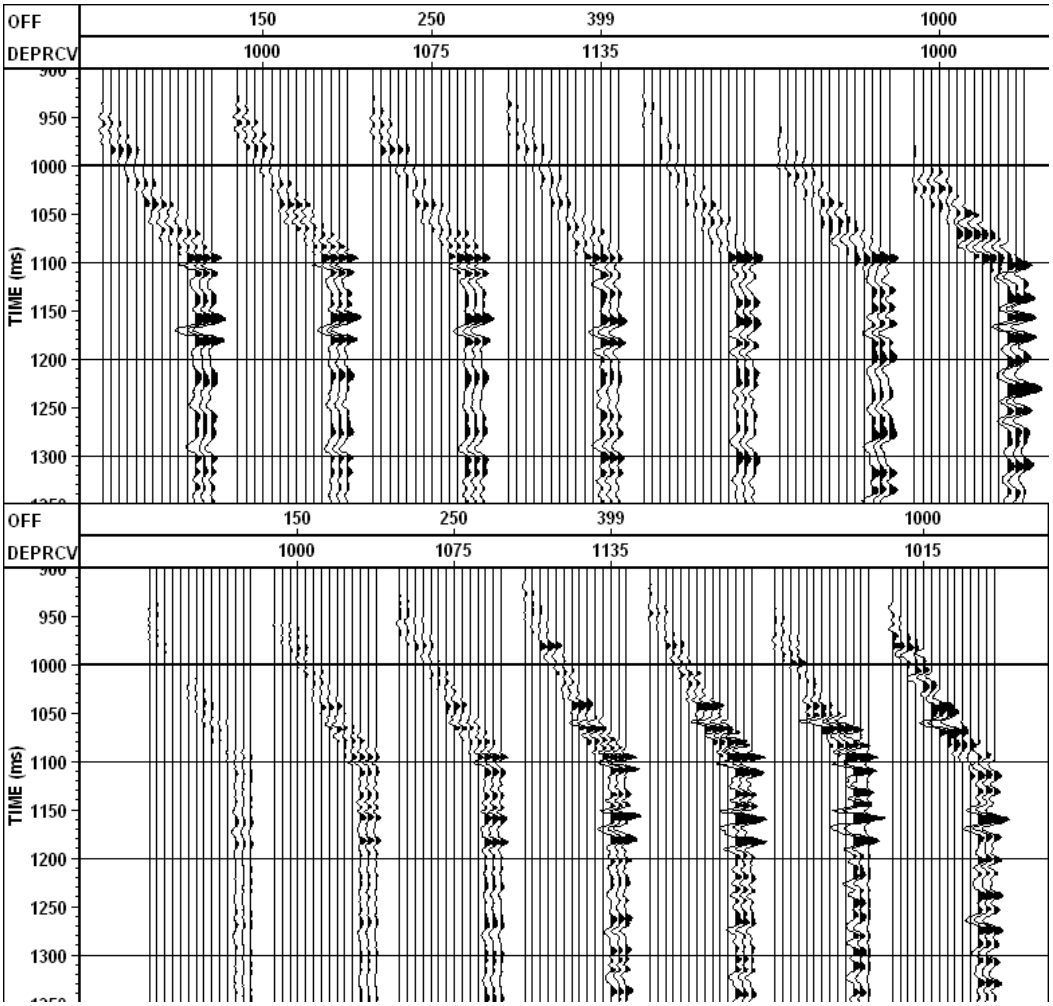

FIG 14. A 50 ms corridor mute to depth 1115m of upgoing P and upgoing SV waves.

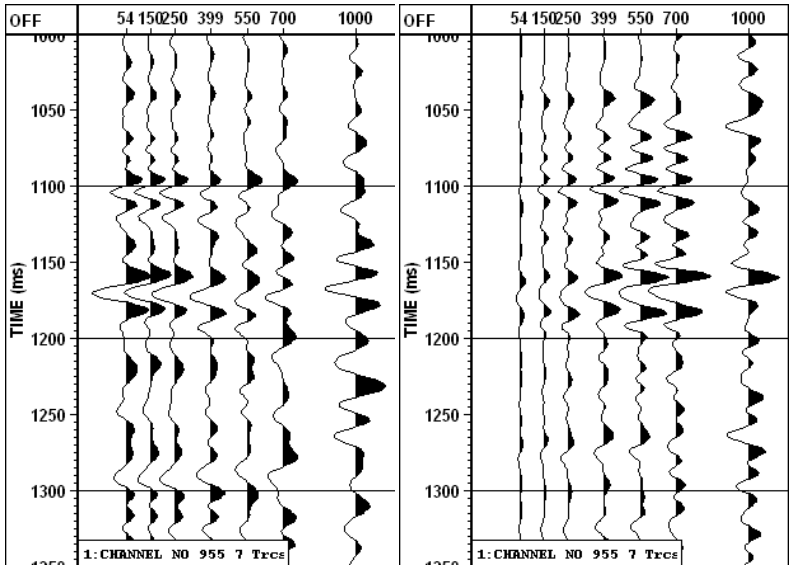

FIG 15. Offset-dependent gathers of upgoing P and upgoing SV waves from corridor stack of each shot.

AVO INTERPRETATION

The composite plots shown in FIG 16 and FIG 17 display the detailed correlation between well logs (gamma ray and velocity as examples) and upgoing P (PP) and upgoing shear (PS) waves from VSP data (the PP data was from the near-offset VSP, the PS data was from the 558 m walkaway VSP shot) within the walkaway VSP receiver depth range. The geological markers for correlation are the top of the Mannville Group, the Cantuar Formation, and the channel sand (the reservoir is in the upper porous sand of the channel). The tops of the Mannville Group and the Cantuar Formation both correlate to peak reflection on PP and PS data on the VSP data. The top of the reservoir appears as a trough on PP reflection, and zero-crossing point (negative to positive) on PS reflection. The bottom of the reservoir expressed as a weak peak reflection on PP data and a zero-crossing point (positive to negative) on PS data.

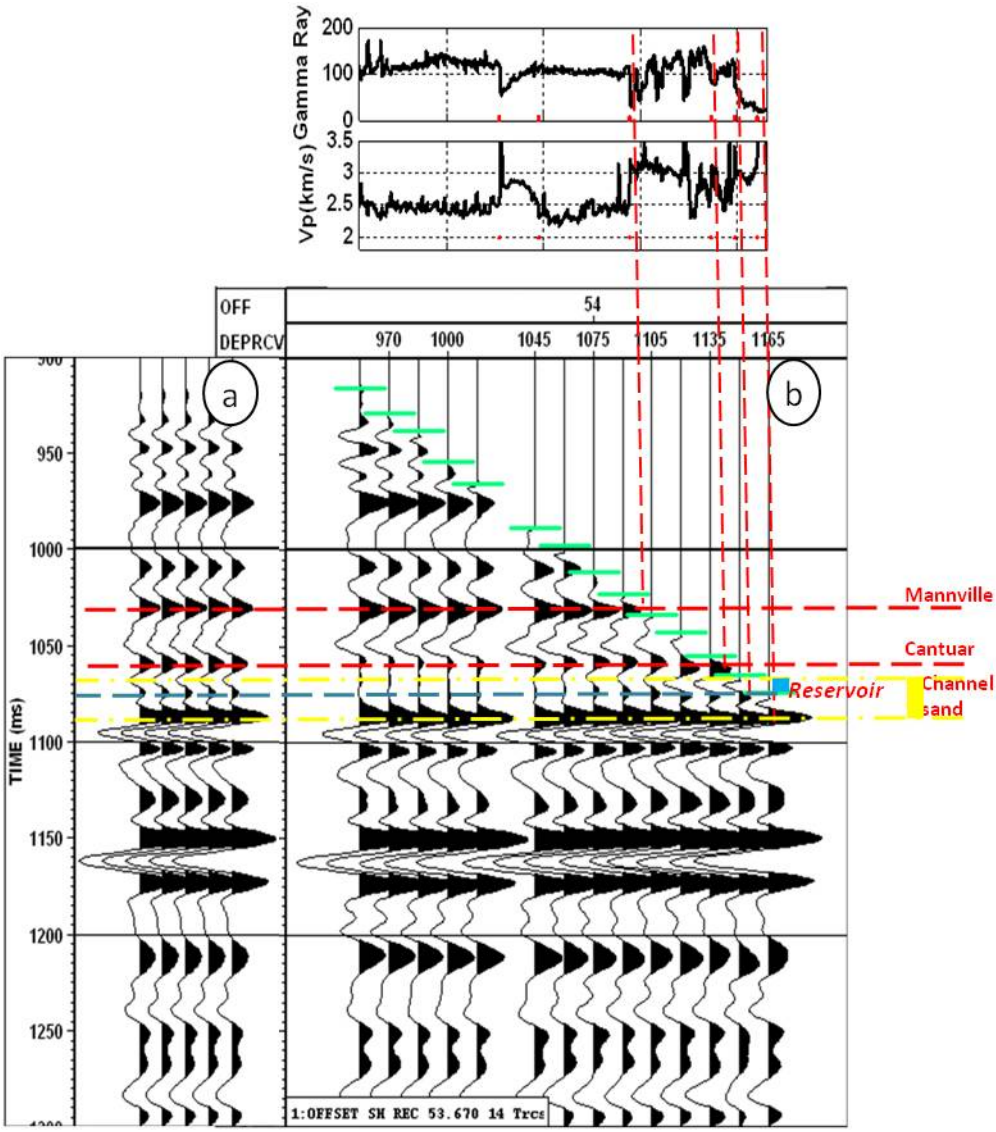

FIG 16. Correlation between well logs and zero-offset VSP within walkaway VSP receiver depth range. a: upgoing P wave corridor stack; b: upgoing P wave in two-way P traveltime (applied NMO and first-arrival time flattening).

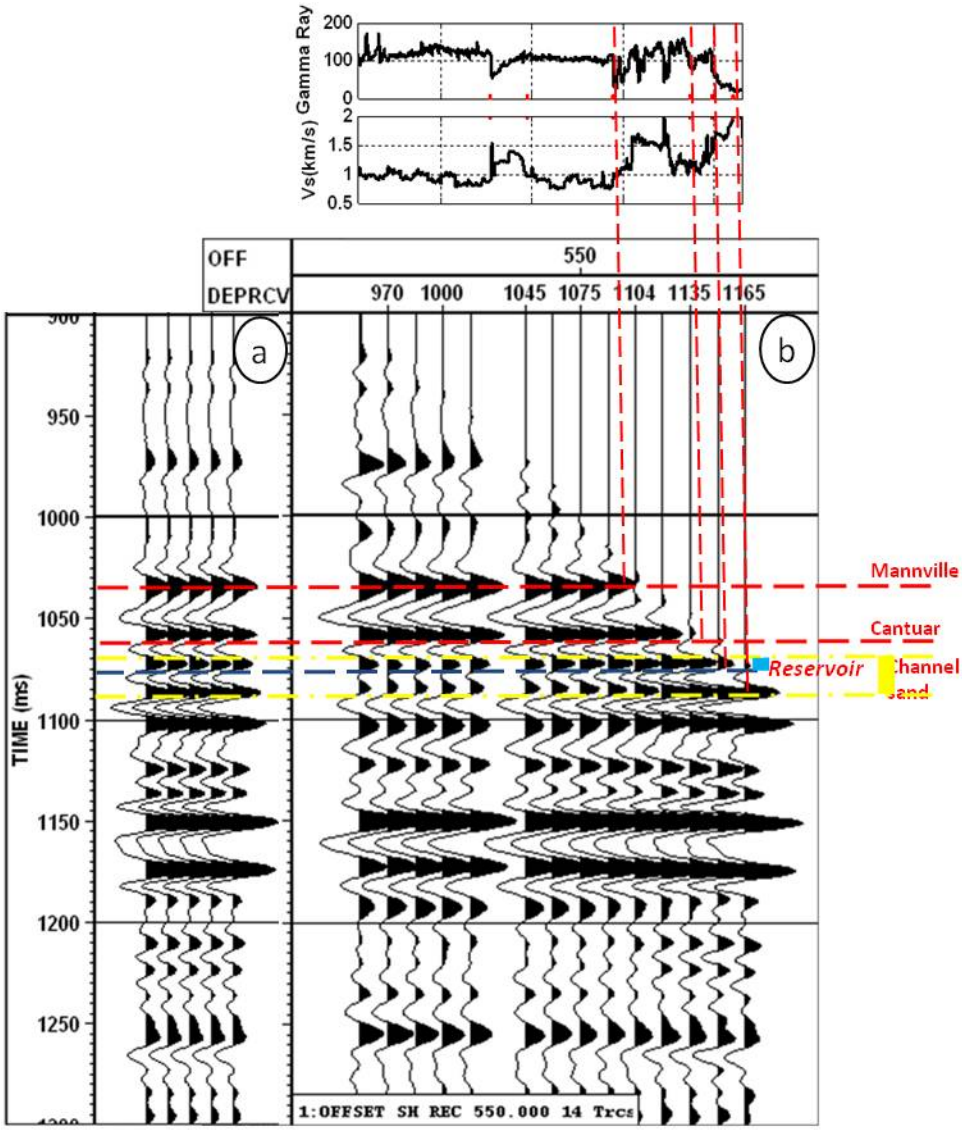

FIG 17. Correlation between well logs and source offset 558 m VSP within walkaway VSP receiver depth range. a: upgoing PS wave corridor stack; b: upgoing PS wave in two-way P traveltime (applied NMO and first-arrival time flattening).

The PP and PS VSP data were then correlated to the synthetic seismograms. FIG 18 displays the correlation of PP data from walkaway VSP data and synthetic seismograms. The synthetic seismograms were generated with VSP calibrated well logs. The corridor stack (FIG 18a) of zero-offset VSP data correlates to the stack trace (FIG 18d) of the synthetic seismogram very well. They display very good event matches, however, there are still amplitude differences between the real and synthetic data. Although the stack was based on the reflection of the base of the channel (1096 ms on PP data), good correlations can still be seen on the reflections of the top and the base of the reservoir. On the synthetic gather (FIG 18c), the top of the reservoir displays an amplitude increase (negative amplitude, here the change means the absolute value variation trend) with offset. The offset gather (FIG 18b) resulting from the walkaway VSP processing displays the same trend except for the

trace at offset 1000 m. At the bottom of the channel sand the VSP offset gather and synthetic gather display the same amplitude decrease (peak) with offset.

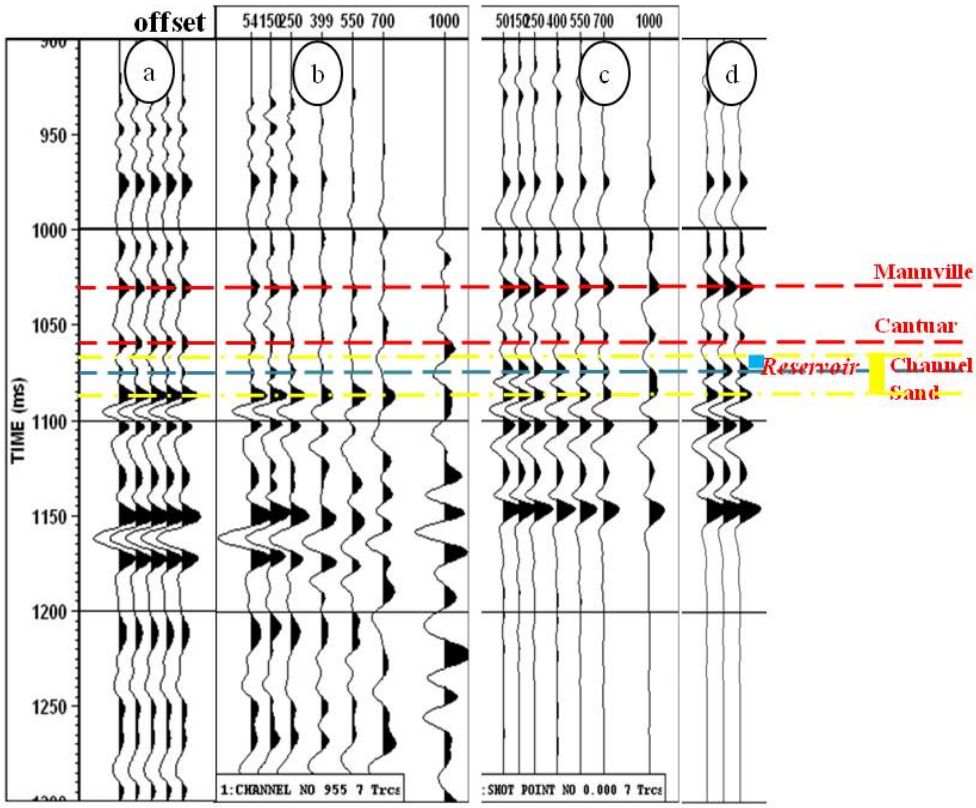

FIG 18. Comparison of PP offset gathers from walkaway VSP processing and PP synthetic seismogram from sonic and density logs. a: upgoing P wave corridor stack of the zero-offset (54 m) VSP (repeated five times); b: PP offset gather from walkaway VSP; c: PP synthetic offset gather; d: stacked traces of the PP synthetic seismogram (repeated three times).

The correlation of PS data from walkaway VSP data and synthetic seismograms is shown as FIG 19. It also displays good correlation between the PS corridor stack (FIG 19a) of offset (558 m) VSP data and the stack trace (FIG 19d) of the PS synthetic seismogram. As found for PP data, good event matches, while amplitude differences between the real and synthetic data are observed. At the top of the reservoir, both the synthetic gather (FIG 19c) and the offset gather (FIG 19b) resulting from the walkaway VSP processing are zero-crossings. At the bottom of the channel sand the VSP offset gather and synthetic gather display the same amplitude increase (peak) with offset.

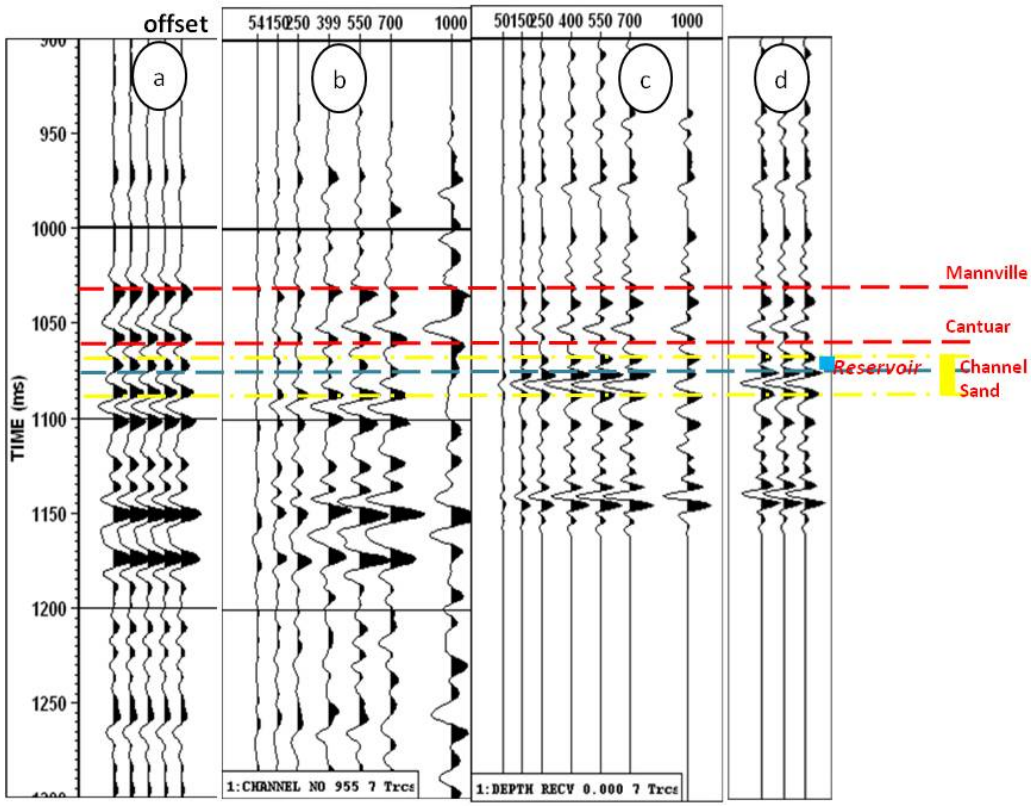

FIG 19. Comparison of the PS offset gather from walkaway VSP processing and PS synthetic seismograms from sonic and density logs. a: upgoing PS wave corridor stack of offset (558 m) VSP (repeated five times); b: PS offset gather from walkaway VSP; c: synthetic PS offset gather; d: stacked traces of the synthetic seismogram (repeated three times). All PS data are plotted in two-way P wave traveltime.

FIG 20 displays the comparison of amplitude versus offset at the base of the channel sand between walkaway VSP data and synthetic seismograms. The amplitudes of synthetic seismograms were scaled to those of the VSP data by multiplying factors deriving from the ratio of average amplitudes of VSP data to those of synthetic data. Both the PP and PS data display similar variation trends of amplitude versus offset. The amplitude differences at each offset are small for both PP and PS data. The mean amplitude difference is 0.2% for PP data, and -0.1% for PS data (Table 2). These results give us promise of rock properties inversion using AVO gather from walkaway VSP.

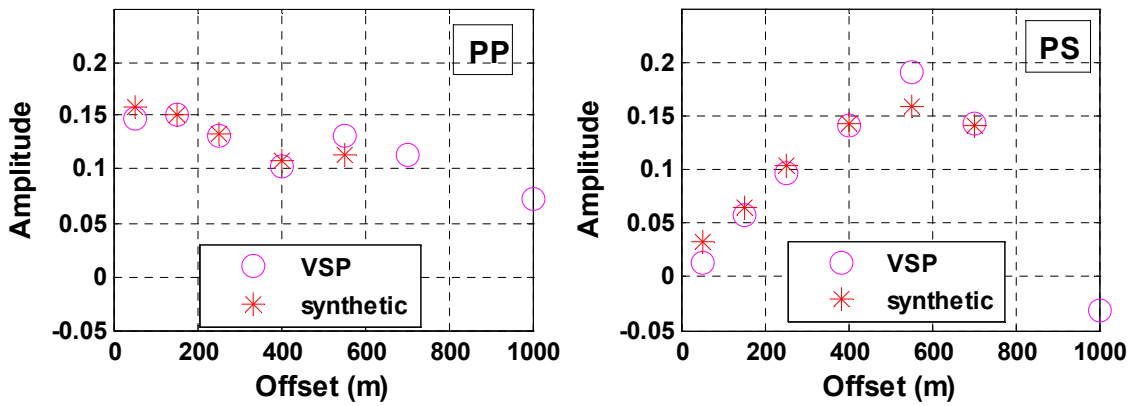

FIG 20. Comparison between the amplitude at the base of the channel sand from walkaway VSP and synthetic seismograms (generated by Syngram) for PP and PS data. The amplitude of synthetic data were scaled to the average amplitude level of VSP data.

Table 2. Amplitude of offset gathers from walkaway VSP data and synthetic seismograms at the base of the channel sand base and their difference.

Amplitude \ Offset (m)		50	150	250	400	550	700	1000
PP	VSP	0.147	0.15137	0.13118	0.10217	0.1313	0.11317	0.07217
	synthetic	0.1577	0.1510	0.1323	0.1082	0.1138	-	-
	mean difference (%)	0.18					-	
	standard deviation (%)	8.45					-	
PS	VSP	0.01303	0.05671	0.09677	0.14156	0.19037	0.14256	-0.0308
	synthetic	0.0326	0.0640	0.01035	0.1428	0.1578	0.1402	-
	mean difference (%)	-	-0.13					-
	standard deviation (%)	-	11.6					-

CONCLUSIONS

The AVO processing and analysis of 3C walkaway VSP data at the Ross Lake heavy oilfield are described in this report. A walkaway VSP geometry has advantages for AVO analysis. True amplitude recovery and wave propagation effects removal are feasible for walkaway VSP data. The use of corridor common-shot stack can improve the signal-to-noise ratio, and minimize undesired wave propagation effect at the same time. At the top and the base of the target channel sand, the synthetic seismogram and walkaway VSP processing results show comparable

amplitude for both PP and PS waves. These results indicate the promise of rock properties inversion using AVO gather from walkaway VSP.

ACKNOWLEDGEMENT

The authors would like to thank GEDCO for donating the VISTA processing package. The support by the sponsors of the CREWES project is gratefully appreciated.

REFERENCES

Blias, E., 2007, VSP wavefield separation: wave-by-wave optimization approach: Geophysics, **72**, T47-T55.

Christopher, J. E., 1974, The Upper Jurassic Vanguard and Lower Cretaceous Mannville Groups of Southwestern Saskatchewan: Department of Mineral Resources: Saskatchewan Geological Survey, Sedimentary Geology Division, Report No. 151.

Coulombe, C.A., Stewart, R.R., and Jones, M.J., 1996, AVO processing and interpretation of VSP data: Canadian Journal of Exploration Geophysics, **32**, 41-62.

Hinds, R. C., and Kuzmiski, R.D., 1996, VSP interpretative processing: theory and practice: Society of Exploration Geophysicists.

Stewart, R.R, and DiSiena, J.P., 1989, The values of VSP in interpretation: The Leading Edge, **8**, 16-23.

Zhang, Z., and Stewart R.R, 2007, VSP processing and analysis at the Ross Lake heavy oilfield, Saskatchewan: 2007 CSEG Annual Convention, Expanded Abstracts.

APPENDIX: HORIZONTAL ROTATION OF 3C VSP DATA

In downhole measurement, the geophone sonde twists and the horizontal components randomly orient from depth to depth. Generally, 3C geophone does not have systems for either downhole orientation or for measuring downhole relative orientation. Thus the coherency of the seismic events of the horizontal components is very poor. FIG A.1 displays the X and Y components of vertical vibrator zero-offset (54m) VSP data. It shows that the horizontal sensors are oriented randomly. Very little coherent signal can be seen on the raw x and y data. It is necessary to orient the horizontal components to consistent directions.

The orientation of horizontal components can be determined by hodogram analysis (Hinds et al., 1996). At each depth level, the angle for the rotation is chosen using a line through the hodogram constructed using the data in a window of one period / cycle after the first arrival. Once the rotation angle is determined, the horizontal components can be rotated into two horizontal directions (FIG A. 2) using equation (1): horizontal radial, Hmax, which is tangent to source-receiver frame, contains most of SV wave and P wave; and horizontal transverse, Hmin, which is orthogonal to source-receiver frame, containing mainly SH wave. The coordinate system of x, y, and z components at the local receiver depth along with the coordinate axis used after rotation are shown in FIG A. 3.

$$\begin{pmatrix} \boldsymbol{Hmax(t)} \\ \boldsymbol{Hmin(t)} \end{pmatrix} = \begin{pmatrix} \boldsymbol{x(t)} & \boldsymbol{y(t)} \end{pmatrix} \begin{pmatrix} \boldsymbol{cos(\theta)} & \boldsymbol{-sin(\theta)} \\ \boldsymbol{sin(\theta)} & \boldsymbol{cos(\theta)} \end{pmatrix} \tag{1}$$

where,

- *Hmax(t), Hmin(t)*: horizontal radial/transverse component;
- *x(t), y(t)*: X, Y components (field record);
- θ: angle between X direction and horizontal radial direction.

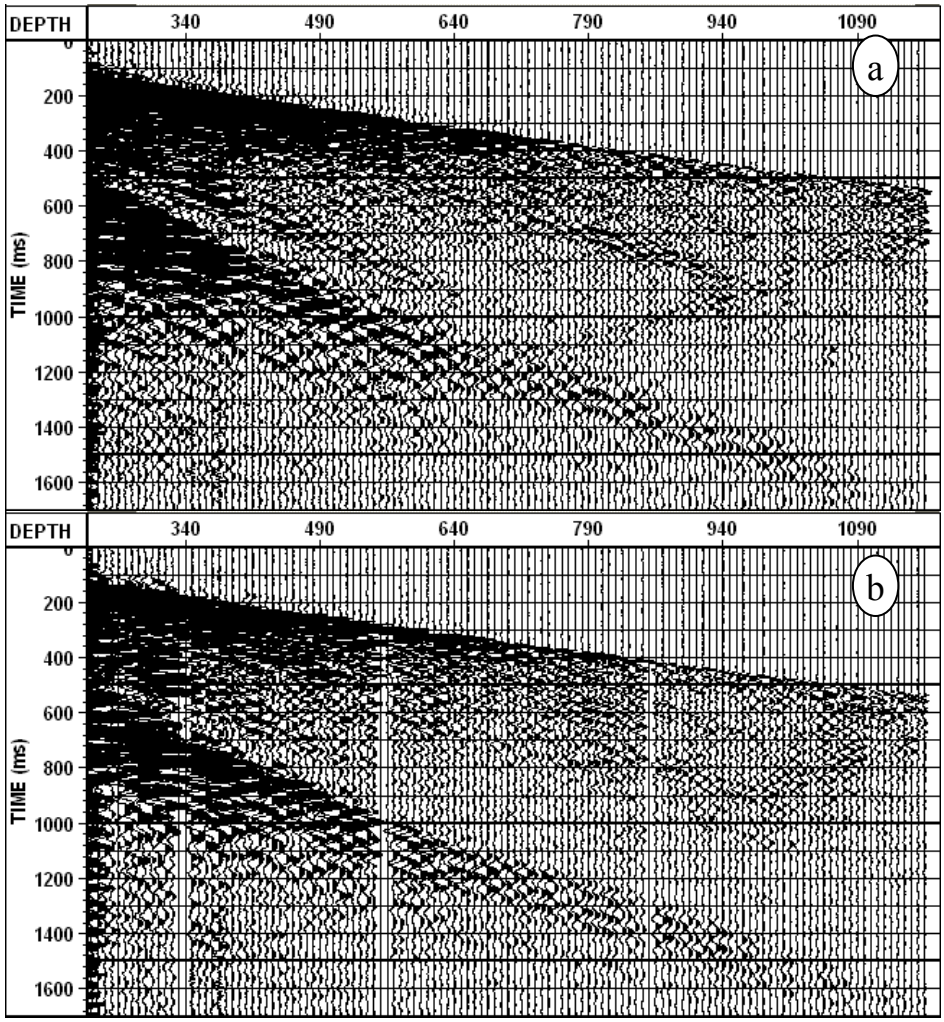

FIG A.1 (a) and Y components (b) of vertical vibrator zero-offset VSP data (source offset 54 m). It shows that the horizontal sensors are oriented in randomly azimuth. Very little coherent signal can be seen on the raw x and y data.

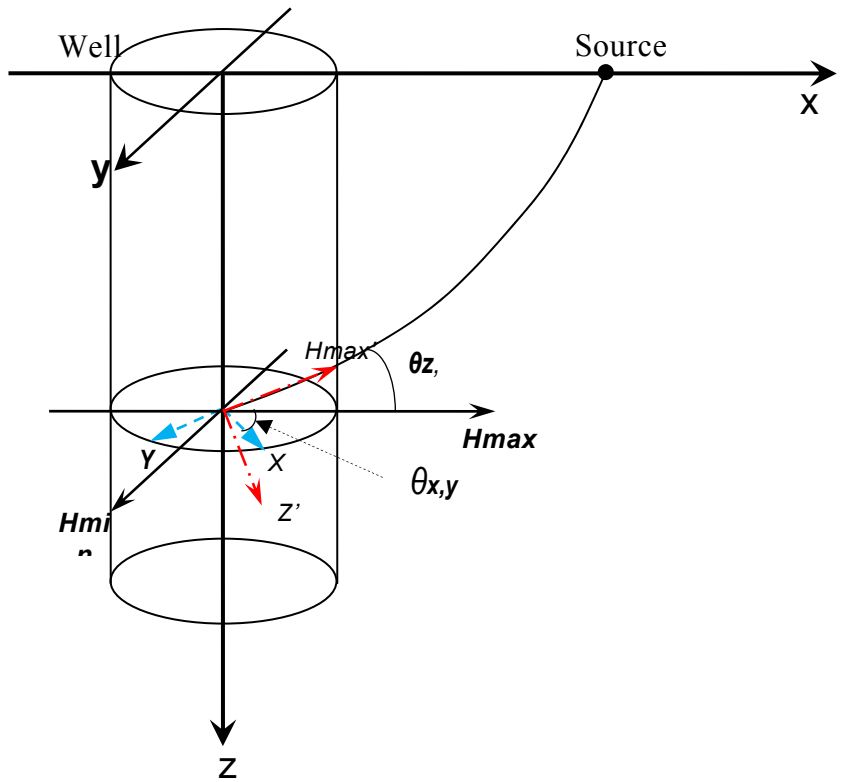

FIG A. 2 The coordinate system of x, y, and z components at the local receiver depth along with the coordinate axis that will be used after rotation (after Hinds et al., 1996).

The Hmax and Hmin from rotation of X and Y components of vertical vibrator zero-offset (source offset 54 m) VSP data are shown in FIG A. 3. Coherent events can be seen on the Hmax and Hmin components. Various wave types, including transmitted, reflected and direct S-waves were also recorded by horizontal receivers (refer to the wave type analysis of zero-offset VSP data in Chapter Two).

FIG A. 4 displays the Hmax, and Hmin from horizontal rotation of X and Y component, and Z components of source offset 699 m VSP. On the horizontal component, transmitted, reflected and direct S-waves can be found. On the vertical component, direct and reflected P-waves can be easily spotted. Comparing with small source offset VSP data, much larger amount of direct S-waves can be seen on vertical component.

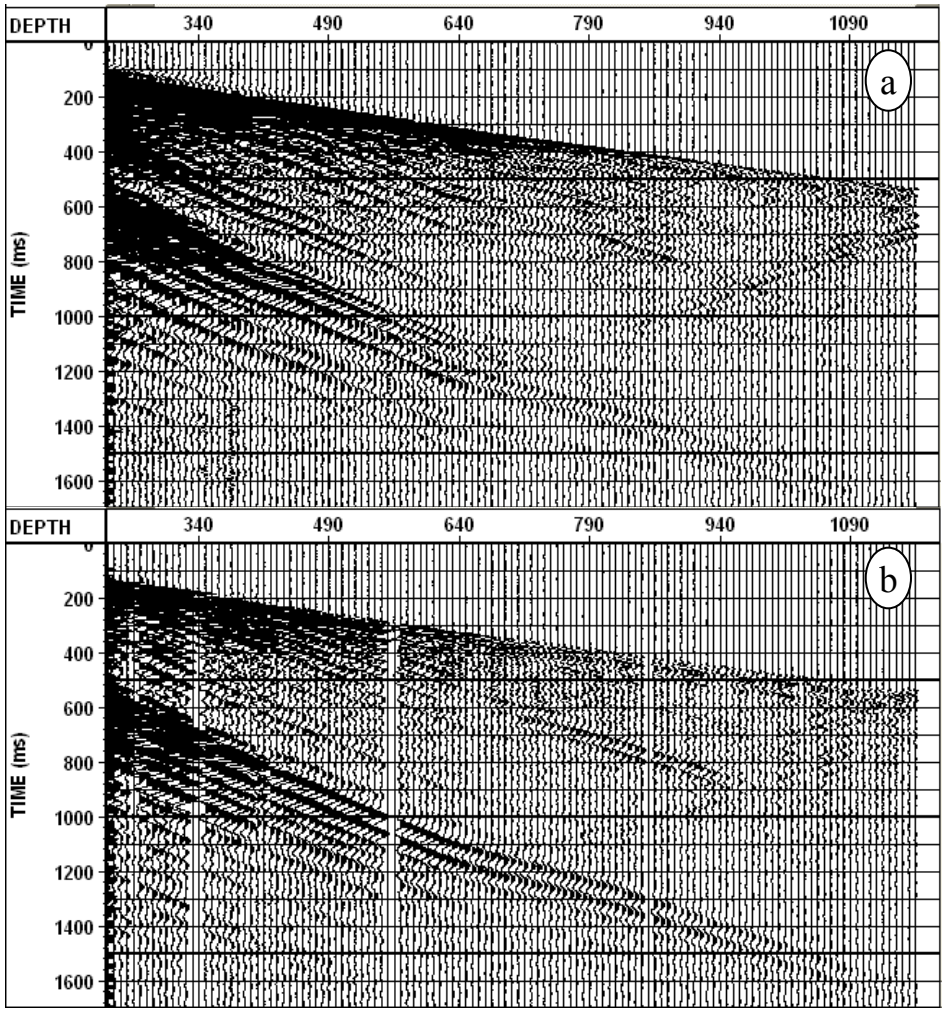

FIG A. 3 Hmax (horizontal radial, a) and Hmin (horizontal transverse, b) of zero-offset VSP (offset 54m, vertical vibrator). Hmax and Hmin are from horizontal rotation of X and Y components.

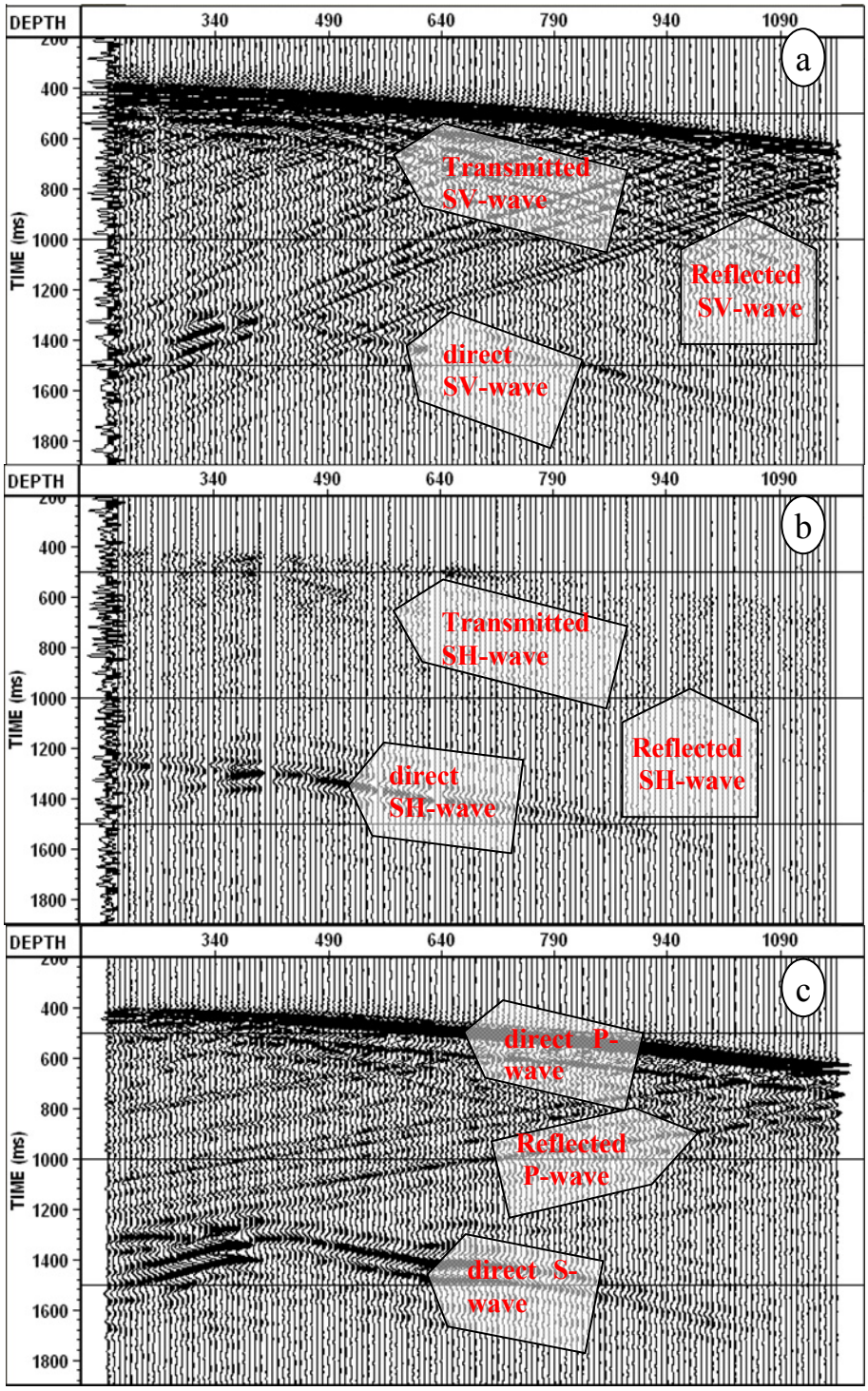

FIG A. 4 Hmax (horizontal radial, a), Hmin (horizontal transverse, b), and Z (c) components of far-offset VSP (offset 699 m). Hmax and Hmin are from horizontal rotation of X and Y components.